Scilight

Regenerative Medicine and Dentistry
https://www.sciltp.com/journals/rmd

Article

Check for updates

Single-Cell Re-Mining Identifies a Pathogenic Fibroblast Subpopulation and Nominates Exploratory Therapeutic Hypotheses in Human Bone Nonunion

Hang Chen [1,2], Chang Lei [2,3], Xiao Liu [4], Xiaobo Chen [5], Shufang Luo [5] and Chun Xu [1,2,6,*]

[1] Sydney Dental School, Faculty of Medicine and Health, The University of Sydney, Sydney, NSW 2006, Australia
[2] Charles Perkins Centre, The University of Sydney, Camperdown, NSW 2006, Australia
[3] School of Medical Science, Faculty of Medicine and Health, The University of Sydney, Sydney, NSW 2006, Australia
[4] Intelligent Polymer Research Institute, Innovation Campus, University of Wollongong, Wollongong, NSW 2522, Australia
[5] Stomatological Hospital of Xiamen Medical College, Xiamen Key Laboratory of Stomatological Disease Diagnosis and Treatment, Xiamen 361000, China
[6] Sydney Nano Institute, The University of Sydney, Sydney, NSW 2006, Australia
* Correspondence: chun.xu@sydney.edu.au

How To Cite: Chen, H.; Lei, C.; Liu, X.; et al. Single-Cell Re-Mining Identifies a Pathogenic Fibroblast Subpopulation and Nominates Exploratory Therapeutic Hypotheses in Human Bone Nonunion. *Regenerative Medicine and Dentistry* **2026**, *3*(2), 7. https://doi.org/10.53941/rmd.2026.100007

Received: 23 February 2026
Revised: 6 April 2026
Accepted: 14 April 2026
Published: 27 April 2026

Abstract: Bone nonunion is a significant clinical problem, yet the cellular mechanisms that sustain failed repair in humans remain poorly understood. Here, we re-analyzed a human nonunion single-cell RNA sequencing (scRNA-seq) dataset to move beyond broad descriptive cell-population changes and generate a subtype-resolved, hypothesis-oriented framework. Across 16 major lineages, differential abundance testing revealed robust expansion of fibroblast, chondrocyte, and macrophage neighborhoods in nonunion. Intercellular communication reconstruction further showed that macrophages were the dominant upregulated signal "senders", whereas fibroblasts were the primary "receivers", with a disease-enhanced macrophage-to-fibroblast TGFB1–(TGFBR1+TGFBR2) axis forming a central hub. Fibroblasts in nonunion also showed metabolic rewiring and an increased senescence signature, including strengthened metabolite-mediated macrophage-to-fibroblast signaling (e.g., glutamine-linked pathways). Further subclustering identified a disease-enriched fibroblast "Fib1 executor" state that acts as a pro-fibrotic signaling sink, governed by a 13-transcription-factor regulon and a compact five-gene effector module (ACTA2, F3, THBS1, SERPINE1, NTM). Finally, we performed an exploratory computational compound-prioritization analysis linked to the Fib1-centered program, generating preliminary hypotheses for future validation rather than validated therapeutic nominations. Together, our results suggest that human nonunion contains a disease-enriched macrophage-to-fibroblast communication program and a fibroblast-centered effector signature that may help guide future mechanistic and therapeutic studies.

Keywords: bone nonunion; single-cell RNA sequencing; fibroblast; drug repurposing

1. Introduction

Bone fracture is one of the most common traumatic injuries worldwide. Physiological fracture healing is a staged program, yet a substantial proportion of long-bone fractures progress to nonunion, commonly cited at ~5–10% depending on bone, injury severity, and treatment context [1]. Clinically, nonunion is often defined as a fracture persisting for at least nine months without radiographic progression for three consecutive months, and it is associated with chronic pain, functional disability, and considerable socioeconomic burden [2]. Large database

and systematic evidence indicate that nonunion markedly escalates healthcare utilization and costs—often several-fold higher than uncomplicated fracture care—and patients experience profound impairment in health-related quality of life [3]. Current management centers on restoring stability and biologic augmentation, but outcomes remain heterogeneous and frequently require repeat procedures [4]. A key barrier is the incompletely defined human intramedullary signaling landscape, where immune–vascular cues and stromal programs may favor fibrotic responses that compete with regeneration [5].

Currently, no authorized pharmacological agents exist for nonunion; care relies on surgical stabilization with or without autologous grafting, which adds donor-site injury [6,7]. Classic human studies depict nonunion tissue as vascularized connective stroma enriched for fibroblasts and CD11b+ macrophages with matrix-remodeling activity, implicating macrophage–fibroblast coupling [8]. Yet the molecular circuitry of the human intramedullary niche remains poorly defined [9]. The published intramedullary scRNA-seq study of human femoral nonunion primarily highlighted altered immune-cell populations, thereby establishing an important cellular reference map but leaving stromal-state heterogeneity and subtype-resolved intercellular communication insufficiently explored [10]. In parallel, other human transcriptomic studies have addressed different biological compartments: La Manna et al. profiled osteoprogenitor cells and identified FOS as a putative regulator of impaired osteogenic repair [11], whereas Salichos et al. compared physiological fracture callus with hypertrophic and oligotrophic nonunion tissues at the bulk transcriptome level [12]. Together, these studies indicate that human nonunion involves both defective regenerative competence and broader tissue-level molecular remodeling, but they do not resolve how immune and stromal states are organized within the disease microenvironment. Accordingly, deeper re-mining of high-resolution human datasets is needed to move beyond broad population-level descriptions and toward subtype-resolved biological hypotheses and target nomination.

In this study, we performed a comprehensive re-analysis of a published human intramedullary scRNA-seq dataset of femoral nonunion, shifting the focus from descriptive cell population changes to a subtype-resolved, hypothesis-generating cell-state framework that helps explain how regenerative programs may become durably impaired in nonunion. Building on evidence that macrophage–fibroblast interactions can sustain chronic fibroinflammatory remodeling, we identified a disease-enriched fibroblast "executor" state with a compact downstream effector suitable for virtual perturbation and target nomination. To extend this biological framework toward future therapeutic hypothesis generation, we integrated this cell-state mapping with an exploratory, repurposing-oriented computational prioritization strategy. Using an integrated machine-learning and structural evaluation workflow, we ranked FDA-approved compounds as preliminary candidates for future validation.

2. Methods

2.1. Public Datasets and Initial Processing

Single-cell sequencing data were downloaded from the Gene Expression Omnibus (GEO) under accession number GSE217792 [10]. The dataset profiles human femur nonunion samples (n = 5) and healthy samples (n = 4) from intramedullary canals. All downstream processing was carried out in R 4.5.0 with Seurat v5 [13] or Python 3.10.4 with OmicVerse [14]. Raw matrices were filtered to retain nuclei/cells with ≥500 expressed genes, ≥1000 unique molecular identifiers (UMIs) and ≤5% mitochondrial transcripts. Putative doublets were identified with scDblFinder [15] and removed. Data were log-normalized (NormalizeData, scale.factor = 1×10^4) and 2000 highly variable features were selected with FindVariableFeatures. Samples were integrated by Harmony software [16]. The integrated matrix was scaled and subjected to principal-component analysis (PCA). The first 30 PCs were used to build a shared nearest-neighbor graph and to generate a two-dimensional UMAP embedding. Louvain clustering (resolution = 1.0) defined transcriptional clusters. Integrated Seurat objects were processed for clustering with standard Seurat 5 workflow. Clusters were labeled as cell types according to characteristic genes identified by Seurat FindMarkers function.

2.2. Composition Analysis

Cell-type frequencies were calculated per sample (prop.table) and visualized by ggalluvial. Transcriptional neighborhoods were calculated by MiloR [17] (k = 30). Neighborhood cell counts were modelled with a negative-binomial generalized linear model that included condition (nonunion vs. control) as a fixed effect; neighborhoods with FDR < 0.1 were deemed differentially abundant. To provide an external cross-dataset comparison with previously published human nonunion transcriptomic studies, we additionally analyzed the public bulk RNA-seq cohort from the GEO GSE226568 [11] super-series, specifically the tissue subseries GSE226566, which includes healthy bone, fracture callus, and nonunion tissue samples. Raw count matrices were processed and deconvolved using BayesPrism [18], with the annotated cell-type reference derived from our scRNA-seq atlas. Inferred cell-

type fractions were summarized at the sample level and compared across groups. Because the external cohort differs from the discovery scRNA-seq dataset in sequencing modality, tissue composition, and cohort structure, this analysis was interpreted as supportive cross-dataset comparison rather than direct orthogonal validation.

2.3. Cell–Cell Communication

Ligand–receptor interactions were inferred with CellChatV2 [19] using the built-in human database. Interactions with $p < 0.05$ (1000 permutations) were retained. Total interaction number, aggregated interaction strength and information-flow metrics were extracted for each condition, and differential interaction matrices (nonunion–control) were visualized as heat maps. To identify macrophage-derived signals influencing fibroblast fate, we applied NicheNet [20], which predicts ligand-receptor interactions driving transcriptional responses by integrating expression data with curated signaling networks.

2.4. Metabolic Inference

The log-normalized, MAGIC-imputed expression matrix for the full atlas (MAGIC, $k = 10$) was analyzed with scFEA [21] using the human metabolic network. Predicted reaction-flux vectors were generated for all cells and retained for downstream analyses. Metabolite-mediated cell-cell communication (mCCC) was reconstructed using MEBOCOST [22] with its curated metabolite–sensor knowledge base. In this framework, sender cells are estimated by metabolite efflux rates together with enzyme expression, and receiver cells by influx rates together with sensor expression; communication chains are reported as sender-to-metabolite-to-sensor-to-receiver. We integrated scFEA-predicted influx/efflux by constraining fluxes via the ConstrainFluxFromAnyTool interface and performed differential mCCC analysis between nonunion and control according to the package's multi-sample comparison options. Unless stated otherwise, significance followed MEBOCOST's default enzyme–sensor co-expression testing; for network display, edges were colored by $\log_2$-fold-change (nonunion vs. control).

2.5. Fibroblast Phenotyping

Fibroblasts were subsetted from the integrated scRNA-seq object and used for state-level phenotyping across control and nonunion conditions. These phenotypic axes were selected to capture fibroblast programs plausibly relevant to nonunion pathophysiology, including migratory remodeling, mechanical matrix sensing, extracellular matrix deposition, contractile/myofibroblast-like activation, senescence-associated dysfunction, and altered cell-cycle states. Cellular senescence was quantified at single-cell resolution using the human Universal Senescence Index (hUSI) [23], generating a continuous senescence score for each fibroblast; fibroblasts were further categorized into senescent versus non-senescent states according to the hUSI algorithm to enable proportion-based comparisons between conditions. Fibroblast cell-cycle state was inferred using Seurat's CellCycleScoring function with canonical S-phase and G2/M-phase gene sets (Seurat cc.genes), which computes per-cell S and G2M scores and assigns discrete phases (G1, S, or G2M). To quantify fibroblast functional polarization, we computed pathway/module activity scores for five phenotype gene sets (Migration, Mechanical signaling, Fibrosis, Myofibroblast differentiation, and Myogenesis) [24] by applying Seurat's AddModuleScore function on curated gene signatures, yielding per-cell module scores that were visualized as ridge plots and compared between control and nonunion fibroblasts. To assess the robustness of the phenotype scoring, we additionally evaluated the same five fibroblast gene signatures using AUCell [25].

2.6. Subtype-Resolved Analysis and Signaling Dynamics

Fibroblasts and macrophages were extracted from the integrated scRNA-seq object and subjected to sub-clustering (resolution = 0.2), yielding four fibroblast states (Fib1–fib4) and three macrophage states (mac1–mac3), which were visualized by UMAP. Subtype-specific markers were identified by differential expression analysis and summarized by volcano plots, followed by integrated GO/KEGG enrichment by metascape [26] to interpret subtype specialization. Intercellular communication was reconstructed using the same CellChat-based signaling inference framework described for macrophage–fibroblast crosstalk, and TGF-β pathway flux was visualized with circle plots; signaling-role importance (Sender/Receiver/Mediator/Influencer) was quantified across representative pathways (TGF-β, FGF, LAMININ, PDGF, ANGPTL). In addition, to directly assess subtype-level targeting of Fib1, we explicitly extracted macrophage-subtype-to-Fib1 interactions from the merged CellChat object and compared them between nonunion and control; pathway-specific contribution analysis was then performed for the TGF-β axis. Fib1-state robustness within the nonunion fibroblast compartment was further evaluated by donor-

level program scoring, parameter perturbation across dimensional settings, clustering resolutions, and leave-one-donor-out reanalysis.

2.7. Regulatory Network Inference and Virtual Perturbation

A Fib1-centered regulatory hierarchy was constructed by integrating a quadrant nomination strategy (genes both Fib1-specific and nonunion-upregulated) with regulon inference. pySCENIC [25] was used to infer TF regulons and rank them by Regulon Specificity Score (RSS); the intersection of top-ranked regulons from all fibroblasts and the Fib1 subset defined 13 potential master regulons, which were assembled into a TF–target network to nominate an effector module. Module activity was quantified by per-cell signature density on the fibroblast UMAP. Functional necessity was evaluated by in silico knockouts at the mRNA level (scTenifoldKnk) [27] and protein-inferred level (scTranslator) [28], followed by GO enrichment of significantly downregulated features.

2.8. Exploratory in Silico Compound Prioritization and Cross-Disease Scoring

To explore whether clinically used compounds might be associated with the Fib1-linked profibrotic program, we implemented an exploratory in silico prioritization workflow integrating deep learning–based drug–target scoring with structure-informed model evaluation. An FDA-approved small-molecule library (from DrugBank) [29] and target protein resources (UniProt) [30], together with drug–target affinity data (ChEMBL) [31], were integrated for screening. NHGNN-DTA [32] was used for the initial triage to rank candidate compounds across the selected Fib1-related protein set. Top-ranked compounds were then further examined using Boltz2-derived structural/model outputs [33]. In this study, we used a prespecified internal cutoff of model score >0.7 across the selected targets as an exploratory prioritization rule for retaining compounds with comparatively stronger predicted interface-level model support within our workflow. This cutoff was used as a heuristic ranking criterion for computational triage only, rather than as an experimental biochemical affinity threshold. Because the nominated Fib1-associated genes include disease-linked effectors/signature components rather than uniformly established conventional small-molecule targets, and because no orthogonal biochemical or cellular target-engagement assays were performed, this workflow was intended for hypothesis generation and prioritization only. Candidate compounds retained by this exploratory framework were subsequently filtered by practical feasibility considerations and further examined against fibrosis-related markers curated from published external studies [34–42].

3. Results

3.1. Single-Cell Landscape and Differential Abundance of Intramedullary Cell Populations in Nonunion

The overall study design is illustrated in Figure 1. To elucidate the cellular heterogeneity and identify critical population shifts within the nonunion microenvironment, we integrated and re-analyzed the published scRNA-seq dataset. Unbiased clustering and Uniform Manifold Approximation and Projection (UMAP) identified 16 major cell lineages, encompassing mesenchymal, immune, and vascular populations (Figure 2A). The identity of these clusters was confirmed through the expression of canonical marker genes, including PDGFRA for fibroblasts, ACAN for chondrocytes, C1QA for macrophages, and LEPR for skeletal stem/progenitor cells (SSPCs) (Figure 2D).

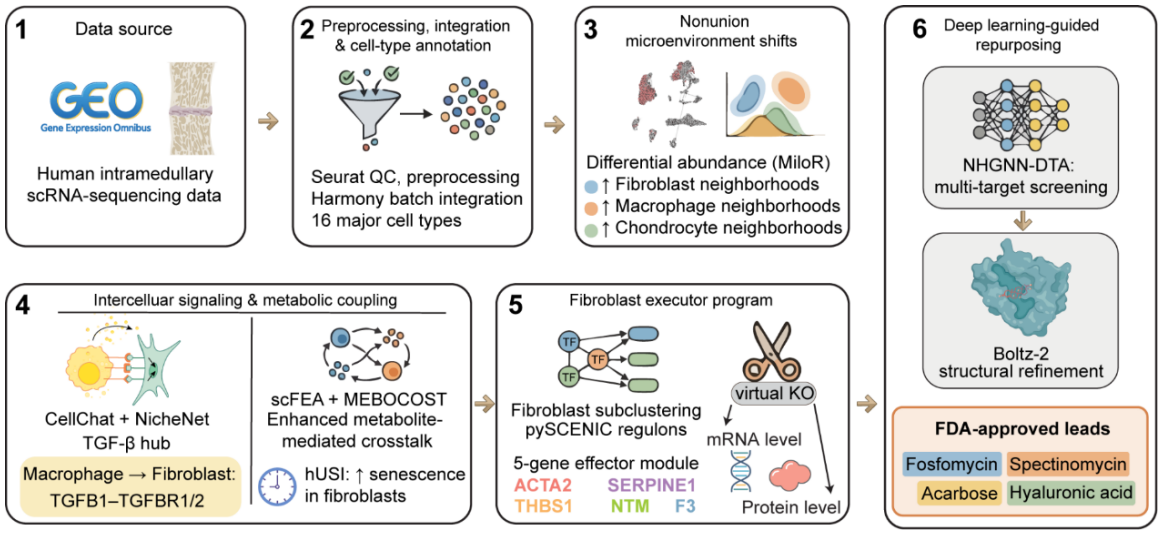

Figure 1. Schematic overview of the study design and analytical workflow.

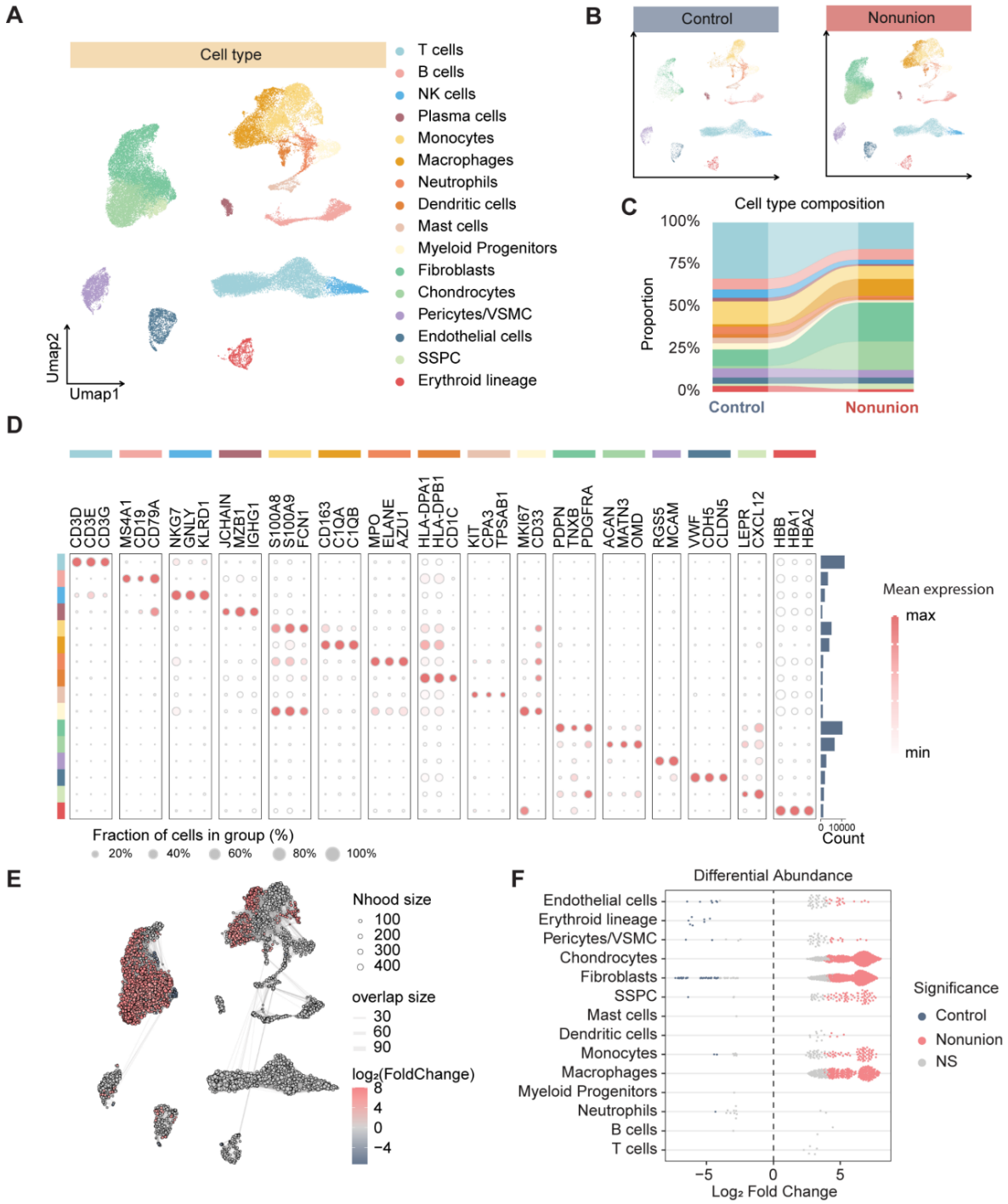

Figure 2. Single-cell landscape and differential cell-type abundance in human intramedullary contents from control and nonunion samples. (**A**) UMAP embedding of the integrated scRNA-seq dataset, with all cells colored by annotated cell type. (**B**) UMAPs split by condition (Control vs. nonunion) to visualize condition-specific distributions of the major cell populations. (**C**) Stacked proportional composition plot summarizing the relative abundance of each annotated cell type in Control and nonunion groups. (**D**) Dot plot of canonical marker genes used for cell-type annotation; dot size denotes the fraction of cells expressing each marker within a cell type, and dot color reflects mean expression (with total cell counts indicated). (**E**) MiloR neighborhood graph over the embedding, illustrating local cell neighborhoods used for differential abundance testing; node size represents neighborhood size, edge thickness reflects neighborhood overlap, and node color indicates the log2 fold-change (nonunion vs. Control). (**F**) Beeswarm summary of MiloR differential abundance results by cell type, showing neighborhood-level log2 fold-changes and significance calls (enriched in Control, enriched in nonunion, or not significant), highlighting expansion/enrichment of macrophage, chondrocyte, and fibroblast neighborhoods in nonunion.

Comparative analysis of the cell type proportions revealed distinct compositional differences between the two conditions (Figure 2B,C). To quantitatively assess these shifts with higher resolution, we employed MiloR for

differential abundance testing across the neighborhood graph (Figure 2E). This analysis revealed a significant expansion of specific cell states in nonunion samples (Figure 2F). Specifically, we observed a robust and statistically significant enrichment of neighborhoods corresponding to fibroblasts, chondrocytes, and macrophages in the nonunion group (Log_2 Fold Change > 0), whereas other populations such as B cells and T cells remained relatively stable (Figure 2F).

Collectively, these findings provide a comprehensive atlas of the nonunion landscape and pinpoint fibroblasts, chondrocytes, and macrophages as the primary expanded populations potentially driving the pathological environment. To assess whether the fibroblast enrichment observed in the discovery single-cell cohort could also be detected in an external dataset, we performed a reference-guided deconvolution of the published bulk RNA-seq cohort from the GSE226568 super-series (tissue subseries GSE226566) using BayesPrism. The inferred cell-type composition profiles varied across healthy bone, fracture callus, and nonunion samples. At the group level, nonunion samples showed a numerically higher inferred fibroblast fraction than healthy bone and fracture callus samples; however, this difference did not reach statistical significance in the external bulk cohort (Figure S1). Thus, the external analysis showed a directionally concordant trend with our single-cell abundance results.

3.2. Elevated Macrophage-to-Fibroblast Crosstalk via the TGF-β Signaling Axis May Define the Nonunion Niche

To investigate the systemic remodeling of intercellular communication that sustains the pathological nonunion environment, we performed integrated signaling analysis using CellChat to infer global and cell-type-specific interaction networks. Comparison of the global signaling architecture between control and nonunion groups revealed an extensive reorganization of the communication landscape (Figure 3A). Differential interaction analysis demonstrated that among the significantly expanded cell populations, macrophages exhibited the most substantial increase in outgoing signal strength (senders), whereas fibroblasts emerged as the primary receivers of these upregulated signals (Figure 3B). To pinpoint the specific molecular drivers of this macrophage-to-fibroblast signaling, we utilized NicheNet to prioritize ligand-receptor pairs based on their potential to induce disease-associated transcriptomic changes. TGFB1 was identified as the top-ranked candidate ligand originating from macrophages, demonstrating high ligand activity and strong interaction potential with receptors expressed on fibroblasts (Figure 3D).

Consistent with this, CellChat differential signaling analysis confirmed a significant increase in the communication probability for the TGFB1–(TGFBR1+TGFBR2) pair in the nonunion group (Figure 3C). Beyond the TGF-β axis, we also observed significantly increased signaling in nonunion for other pro-fibrotic and inflammatory pairs (Figure 3C), including SPP1–CD44, FN1–integrins, and TNFSF12–TNFRSF12A, and related pairs. Pathway-restricted visualization of the TGF-β signaling network within the macrophage-fibroblast-chondrocyte triad revealed that the signaling flux is predominantly directed from macrophages toward fibroblasts, with negligible interaction observed toward chondrocytes (Figure 3E).

To examine whether the predicted axis was reflected at the transcript level, we compared the expression of key components using a two-sided Wilcoxon rank-sum test. In the nonunion microenvironment, macrophages expressed significantly higher levels of the ligand TGFB1 compared to fibroblasts, while fibroblasts exhibited markedly higher expressions of the receptors TGFBR1 and TGFBR2 (Figure 3F). Collectively, these observations are consistent with a disease-enhanced macrophage-to-fibroblast TGF-β signaling axis.

3.3. Multidimensional Characterization Reveals Metabolic and Phenotypic Shifts in Nonunion Fibroblasts

To delineate functional programs that accompany fibroblast expansion and activation in nonunion, we profiled cell-type and condition-specific metabolic states and fibroblast phenotypic polarization at single-cell resolution. We inferred metabolic fluxes using scFEA, reconstructed metabolite-mediated intercellular communication using MEBOCOST, and quantified fibroblast senescence (hUSI), cell-cycle distribution, and pathway activity scores. scFEA revealed condition-dependent metabolic reprogramming in both fibroblasts and macrophages, including increased flux through glutathione-associated and TCA-linked modules in nonunion fibroblasts (Figure 4A). Consistent with a communication-relevant metabolic shift, MEBOCOST identified strengthened macrophage-to-fibroblast metabolite signaling in nonunion, with predominantly increased metabolite–sensor edges, exemplified by L-glutamine–SLC38A2, choline–SLC44A1, and riboflavin–SLC52A2 interactions (Figure 4B).

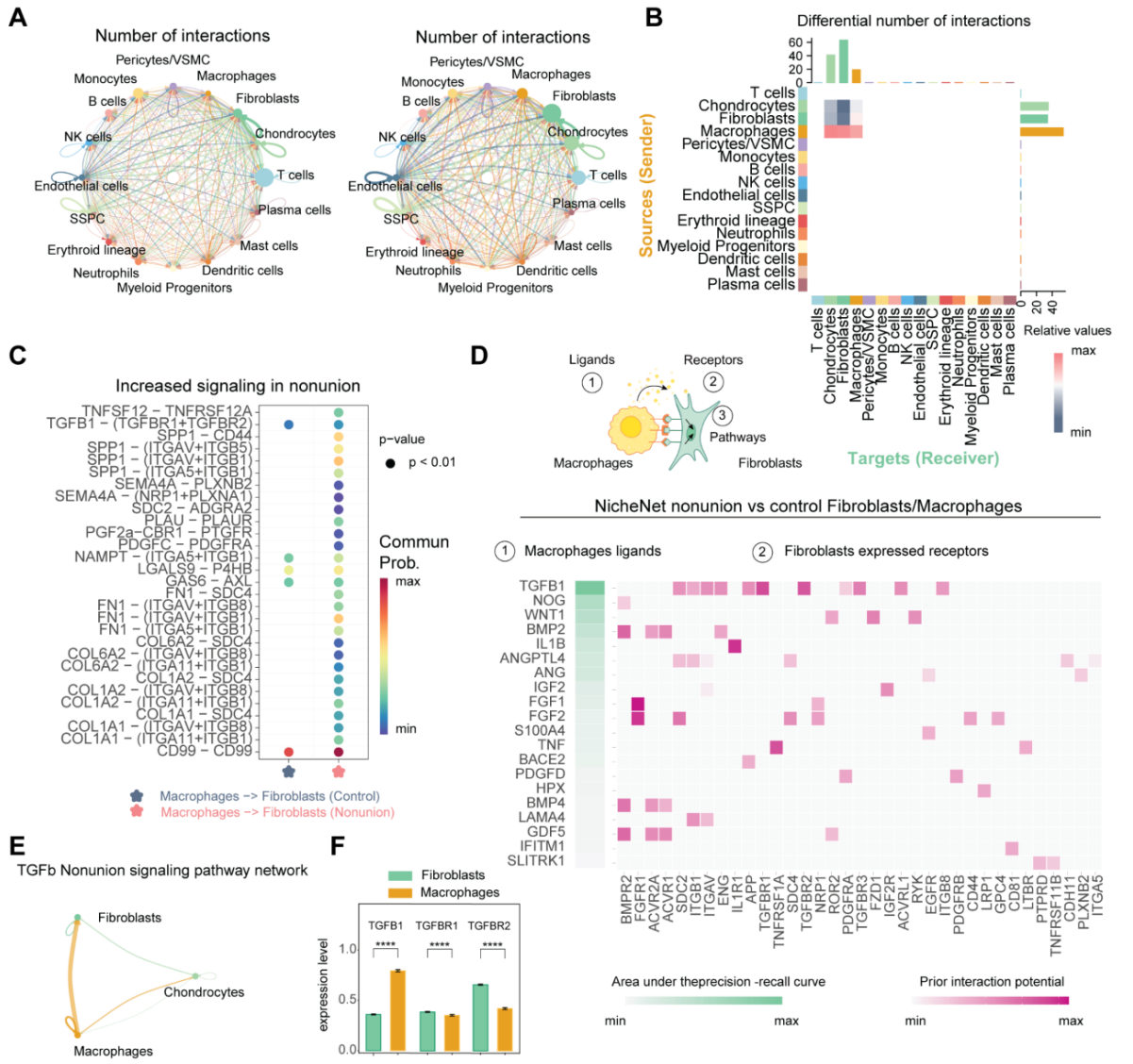

Figure 3. Cell–cell communication remodeling in nonunion. (**A**) CellChat-inferred global intercellular communication networks shown separately for Control (left) and nonunion (right), with edge weights reflecting the number of inferred interactions between sender and receiver cell types. (**B**) Heatmap summarizing the differential number of inferred interactions between cell types (senders vs. receivers), highlighting communication changes involving the three cell populations expanded in nonunion (macrophages, fibroblasts, and chondrocytes). (**C**) CellChat differential signaling analysis identifying ligand–receptor interactions increased in nonunion (bubble color indicates communication probability; dot size indicates significance threshold as displayed), including macrophage-to-fibroblast interactions such as TGFB1–(TGFBR1+TGFBR2) and additional ECM/adhesion- and cytokine-related pairs. (**D**) NicheNet ligand–receptor prioritization for macrophage-to-fibroblast communication in nonunion versus Control, integrating ligand activity (area under the precision–recall curve) with prior interaction potential to rank candidate macrophage ligands and fibroblast-expressed receptors. (**E**) CellChat network visualization of the TGF-β signaling pathway in nonunion restricted to macrophages, fibroblasts, and chondrocytes. (**F**) Bar plots comparing mRNA expression of TGFB1, TGFBR1, and TGFBR2 between macrophages and fibroblasts. *p* values were calculated using a two-sided Wilcoxon rank-sum test.

We next mapped fibroblast state changes and observed heterogeneous hUSI signals across the embedding (Figure 4C), accompanied by a marked increase in the proportion of hUSI-classified senescent fibroblasts in nonunion compared with control ($p < 0.001$) (Figure 4D). Cell-cycle profiling further demonstrated a redistribution characterized by reduced G1 and increased G2M fractions in nonunion fibroblasts ($p < 0.001$) (Figure 4E), indicating altered cell-cycle state distribution in nonunion fibroblasts, with relative enrichment of the G2M-associated fraction rather than definitive evidence of productive proliferation.

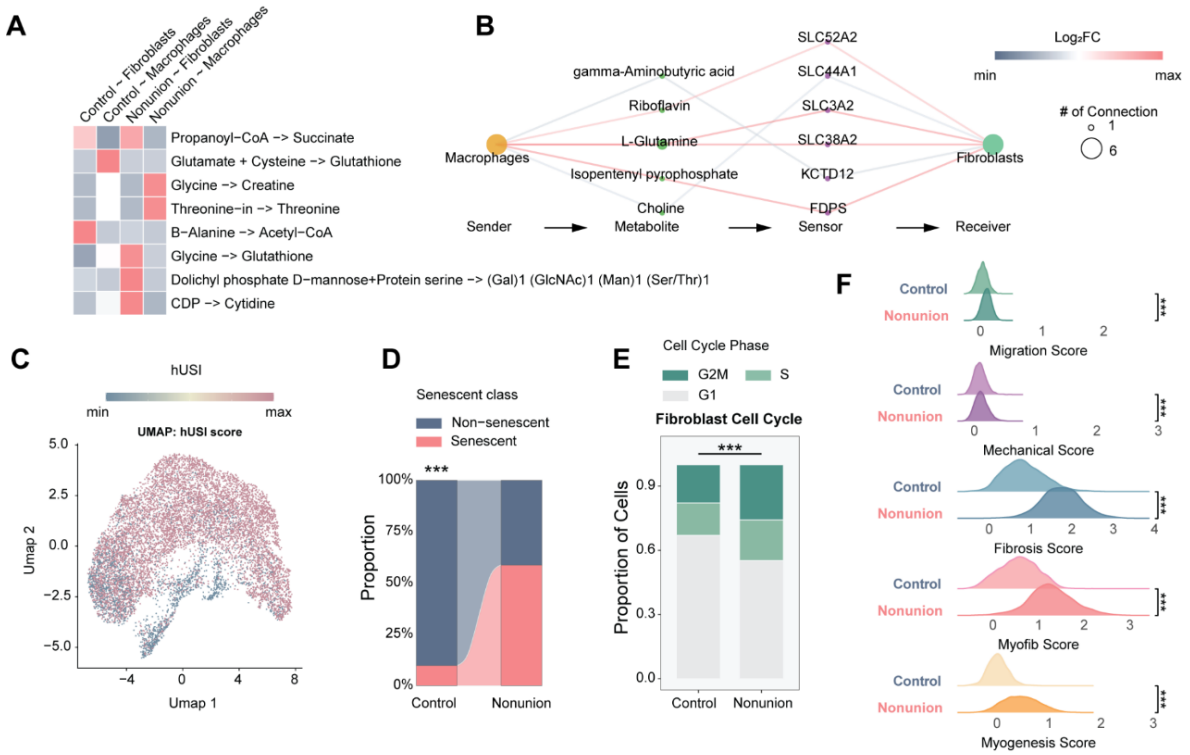

Figure 4. Metabolic reprogramming and accelerated senescence in fibroblasts characterize the nonunion microenvironment. (**A**) scFEA-based metabolic flux inference highlighting the top-ranked, group-specific differential metabolic reactions/flux modules (i.e., features showing the largest between-group differences as ranked in the analysis), visualized to compare metabolic activity patterns across the indicated groups. (**B**) MEBOCOST-based metabolic communication network illustrating signaling from macrophages (senders) to fibroblasts (receivers) through specific metabolites (e.g., L-Glutamine, Choline) and their corresponding sensors (e.g., SLC38A2, SLC44A1). Node size represents the number of connections; edge color indicates Log_2Fold Change (Log_2FC). (**C**) UMAP projection of the fibroblast population colored by the human Universal Senescence Index (hUSI) score, reflecting individual cell senescence levels. (**D**) Bar plot showing the proportion of senescent vs. non-senescent fibroblasts in Control and Nonunion groups classified by the hUSI algorithm. (**E**) Stacked bar plot comparing the distribution of fibroblast cell cycle phases (G1, S, and G2M) between groups. (**F**) Ridge plots comparing functional pathway scores (Migration, Mechanical, Fibrosis, Myofib, and Myogenesis) between control and Nonunion fibroblasts by "AddModuleScore".

Finally, pathway scoring revealed elevated migration-, mechanical signaling–, myogenesis-, fibrosis-, and myofibroblast differentiation–associated programs in nonunion fibroblasts (all $p < 0.001$) (Figure 4F). AUCell-based analysis showed an overall concordant nonunion-versus-control pattern across these phenotype signatures, with clearer separation for mechanical signaling, myogenesis, fibrosis, and myofibroblast differentiation, and a more modest difference for cell migration (Figure S2). Together, these analyses indicate that nonunion fibroblasts adopt a senescence-enriched, metabolically reprogrammed, and functionally pro-fibrotic state, while macrophage-to-fibroblast metabolite signaling is concurrently intensified, providing an orthogonal metabolite-level layer that supports disease-associated remodeling of intercellular communication.

3.4. Subtype-Resolved Analysis Identifies a Recurrent Fib1-Like Fibroblast State Associated with Pro-Fibrotic Signaling in Nonunion

To resolve the functional heterogeneity within the expanded intramedullary populations, we performed high-resolution sub-clustering, which delineated four fibroblast (Fib1–fib4) and three macrophage (mac1–mac3) transcriptional states (Figure 5A,B). Differential expression analysis identified highly distinct molecular signatures for each sub-population. Specifically, Fib1 was labeled by a suite of pro-fibrotic and stress-response markers, including SERPINE1, PHLDA2, and TIMP1, whereas fib2 and fib4 expressed genes related to vascular homeostasis such as CTSH and SNCG (Figure 5C). Within the myeloid compartment, mac2 emer ged as a disease-relevant cluster characterized by the expression of INHBA and CCL7 (Figure 5C).

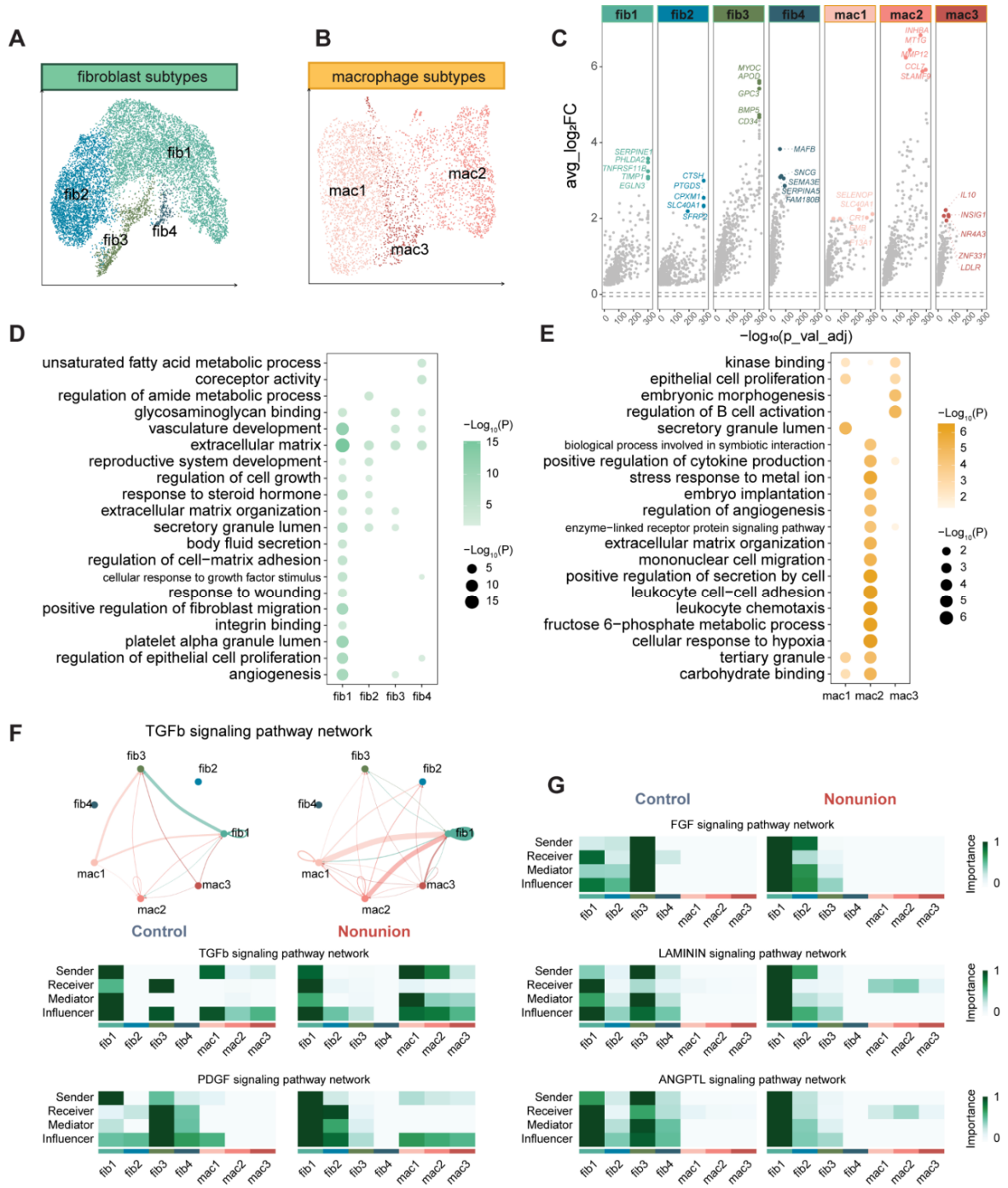

Figure 5. Identification of fibroblast and macrophage subpopulations and their intercellular signaling dynamics. (**A**,**B**) UMAP visualization of (**A**) fibroblast subtypes (Fib1–fib4) and (**B**) macrophage subtypes (mac1–mac3) identified by sub-clustering of the single-cell transcriptomic data. (**C**) Volcano plots displaying subtype-specific differentially expressed genes (DEGs) for each identified cluster. The top five significantly upregulated genes for each subtype are highlighted. The *x*-axis represents average $\log_2$FC and the y-axis represents $-\log_{10}$(adj. *p*-value). (**D**,**E**) Dot plots illustrating Gene Ontology (GO) enrichment terms for fibroblast (**D**) and macrophage (**E**) subtypes. The color intensity and dot size represent the significance level. (**F**) Intercellular communication networks (circle plots) for the TGF-β signaling pathway, comparing interaction strengths between Healthy (Control) and Nonunion groups. (**G**) Heatmaps identifying the importance of signaling roles (Sender, Receiver, Mediator, and Influencer) for five representative pathways: TGF-β, FGF, LAMININ, PDGF, and ANGPTL. The relative contribution of each cell subtype (Fib1–4 and mac1–3) is compared between Control and Nonunion conditions.

Functional interpretation via GO and KEGG enrichment analysis revealed profound specialization across these subtypes. Fib1 was uniquely enriched for pathways essential to fibrosis progression, including “extracellular matrix organization”, “positive regulation of fibroblast migration”, and “integrin binding”. In contrast, fib4 showed

metabolic specialization in "unsaturated fatty acid metabolic processes", suggesting these subtypes perform supportive rather than primary pathological roles. Among macrophages, mac2 displayed a hyper-active profile enriched in "leukocyte chemotaxis", "positive regulation of cytokine production", and notably, "cellular response to hypoxia". This suggests that mac2 acts as the primary inflammatory engine within the hypoxic nonunion microenvironment.

To bridge these subtype identities with intercellular communication, we mapped signaling roles across condition-specific networks. Circle plots of the TGF-β signaling pathway demonstrated that in the nonunion group, signaling density markedly increased, with flux primarily directed from all macrophage subtypes—particularly the mac1 and mac2—toward Fib1. Further quantification of signaling importance (Sender, Receiver, Mediator, and Influencer) suggested this pattern across FGF, LAMININ, PDGF, and ANGPTL pathways. In the nonunion state, Fib1 consistently exhibited increased "Receiver" and "Influencer" importance scores compared with the control group, whereas mac1 and mac2 retained dominant "Sender" roles, especially in TGF-β signaling. To directly address whether macrophage-derived signals preferentially target Fib1 at the subtype level, we specifically extracted macrophage-subtype-to-Fib1 interactions from the subtype-resolved CellChat analysis. This direct comparison showed increased signaling from macrophage subtypes to Fib1 in nonunion relative to control (Figure S3A), with TGF-β emerging as a representative contributing pathway (Figure S3B). Collectively, these analyses support a subtype-resolved macrophage-to-Fib1 signaling bias in nonunion, with Fib1 behaving as a preferential recipient state rather than establishing direct causal proof of Fib1 state induction.

To assess whether this Fib1-associated program was robust to analytical perturbation rather than being tied to a single clustering configuration, we performed complementary reproducibility analyses within the nonunion fibroblast compartment (Figure S4). Donor-level analysis showed that the Fib1 program was detectable across nonunion donors, although its magnitude varied between specimens (Figure S4A). Across alternative clustering resolutions and dimensional settings, the best-matching recovered cluster retained substantial similarity to the original Fib1 reference program, supporting robustness to reasonable parameter changes (Figure S4B). Leave-one-donor-out analysis further showed that a Fib1-like state remained recoverable after sequential exclusion of each nonunion donor, arguing against the possibility that the signal was driven solely by a single donor (Figure S4C). Together, these analyses support interpretation of Fib1 as a recurrent disease-enriched fibroblast state/program rather than a dataset-specific clustering artifact.

3.5. Integrated Regulon-Target Analysis Identifies a Potential Core TF-Driven Signature Governing the Fib1 Pathological Program

To elucidate the transcriptional control architecture of the disease-associated Fib1 subtype, we integrated subtype-resolved marker profiling, regulon prioritization, and downstream target perturbation. Differential expression analysis first confirmed that the Fib1 subtype possesses a highly specific transcriptomic signature (Figure 6A). To align subtype specificity with disease relevance, we utilized a quadrant plot correlating Fib1 specificity (Fib1 vs. others) with disease-associated differential expression (Nonunion vs. control), identifying a cohort of genes that are both highly specific to Fib1 and significantly upregulated in nonunion (Figure 6B).

We next sought to identify the upstream master regulators of this program using pySCENIC. Ranking transcription factor (TF) regulons by Regulon Specificity Score (RSS) identified distinct regulatory landscapes for both the total fibroblast pool and the Fib1 subtype (Figure 6C). The intersection of the top-ranked regulons from both analyses yielded 13 core master regulons, including SOX9(+), PRRX2(+), TBX15(+), RARG(+), EGR1(+), and SMAD5(+) among representative regulators (Figure 6D). To pinpoint the most critical effectors within the Fib1 program, we constructed a TF-target network based on these 13 master regulons. By marking targets within the network that were also identified in our quadrant analysis as both Fib1-specific and nonunion-upregulated, we successfully discovered five key target genes: F3, THBS1, SERPINE1, ACTA2, and NTM (Figure 6E). The composite signature density of these five key targets was uniquely concentrated within the Fib1 territory in UMAP space, further validating their role as a robust molecular signature for this pathological subtype (Figure 6F).

Finally, we performed in silico perturbation using scTenifoldKnk (mRNA level) and scTranslator (protein level) to simulate the knockout (KO) of these five key targets (Figure 6G). Virtual perturbation of this signature led to a profound downregulation of a network of genes critical to nonunion pathology (Figure 6G). GO enrichment analysis of the significantly downregulated features revealed a primary concentration in pathways related to "extracellular matrix organization", "skeletal system development", and "collagen trimer" (Figure 6H). Collectively, these results support a putative regulatory hierarchy in which 13 core transcription factors may converge on a 5-gene effector signature associated with the fibrotic microenvironment in nonunion.

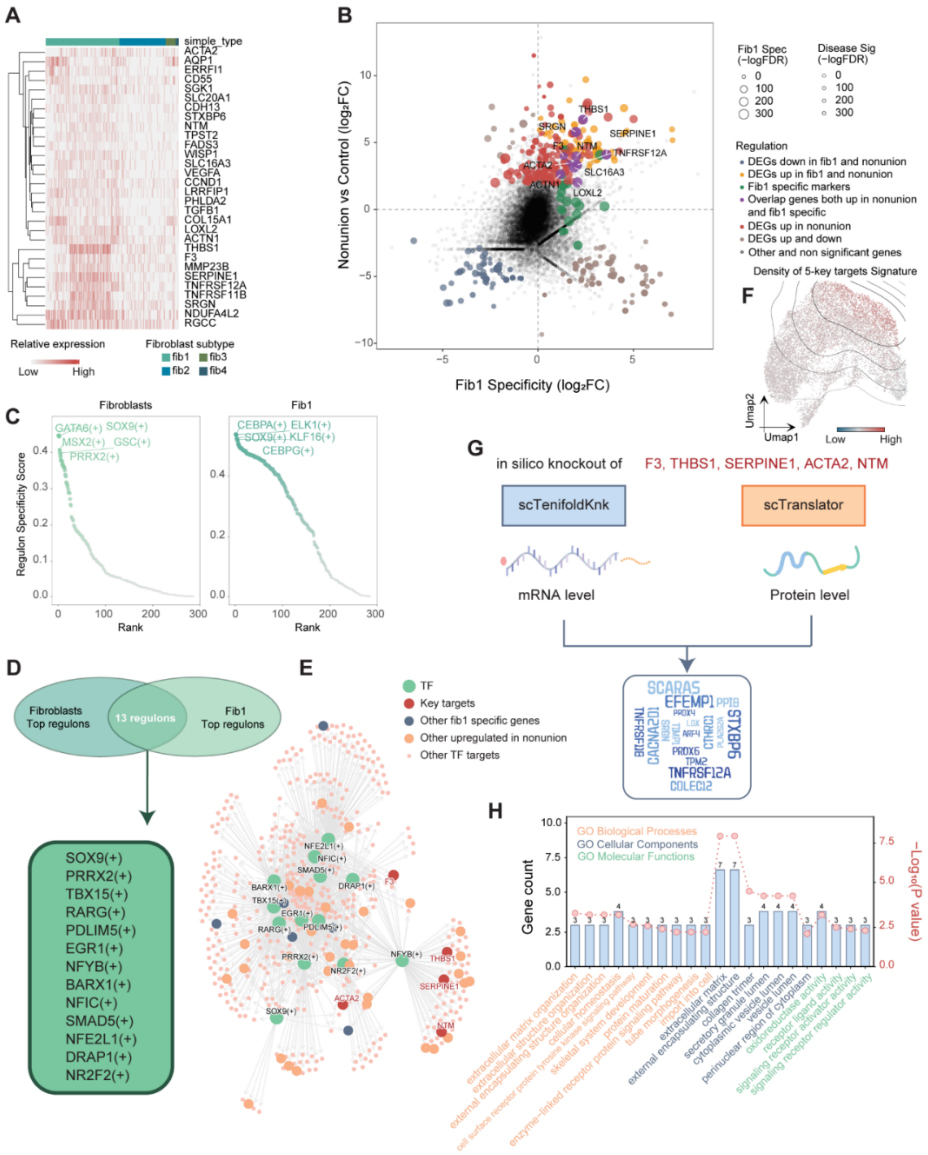

Figure 6. Identification and validation of the master regulatory network driving the Fib1 subtype in nonunion. (**A**) Heatmap showing the relative expression of top Fib1 marker genes across the four identified fibroblast subtypes (Fib1–fib4), demonstrating high subtype specificity for Fib1. (**B**) Quadrant plot correlating disease-associated differential expression (log_2FC Nonunion vs. Control) with cluster specificity (log_2FC Fib1 vs. others). Red dots highlight key genes simultaneously upregulated in nonunion and specific to the Fib1 subtype (e.g., THBS1, SERPINE1, ACTA2, NTM, and F3). (**C**) Rank plots of Regulon Specificity Scores (RSS) for TFs in all fibroblasts (left) and the Fib1 subtype (right), identifying top candidate master regulators. (**D**) Venn diagram illustrating the intersection of the top regulons from all fibroblasts and the Fib1 subtype, with the 13 common master regulons (including SOX9, PRRX2, and EGR1) listed (**E**) Transcription factor-target gene network based on pySCENIC analysis. Green nodes represent TFs; red nodes indicate the 5 key targets upregulated in nonunion and Fib1-specific; dark blue nodes represent other Fib1-specific markers; and orange nodes represent genes upregulated in nonunion. (**F**) UMAP plot displaying the density score of the 5-key target signature (F3, THBS1, SERPINE1, ACTA2, NTM) across the fibroblast landscape. (**G**) Workflow for the in silico knockout (KO) of the five key targets using scTenifoldKnk (mRNA level) and scTranslator (protein level). The resulting word cloud displays downstream genes affected by the virtual KOs, where font size represents the frequency of significant downregulation across the five KO simulations. (**H**) Gene Ontology (GO) enrichment analysis (Biological Process, Cellular Component, and Molecular Function) of the genes significantly downregulated following in silico knockout of the key targets.

3.6. Exploratory Computational Prioritization Highlights Compounds Associated with the Fib1-Linked Profibrotic Program

To explore whether clinically used compounds might be computationally prioritized in relation to the Fib1-linked profibrotic signature (ACTA2, F3, NTM, SERPINE1, and THBS1), we implemented an exploration in

silico prioritization workflow across the selected Fib1-associated protein set (Figure 7A). We initially screened a library of FDA-approved small molecules from the DrugBank database using NHGNN-DTA, which was fine-tuned with ChEMBL-derived drug-target affinity data and UniProt structural resources (Figure 7A). This initial phase prioritized the top 20 candidate drugs based on aggregated predicted multi-target scores. To further refine the prioritization of the top 20 candidates, we used Boltz2-derived structural/model outputs to evaluate these compounds (Figure 7B). Using the Boltz2-derived model score as an internal exploratory ranking metric, we found that while most molecules exhibited heterogeneous target-wise performance, seven drugs exceeded the prespecified inclusion threshold of model score > 0.7 across all five targets (Figure 7B).

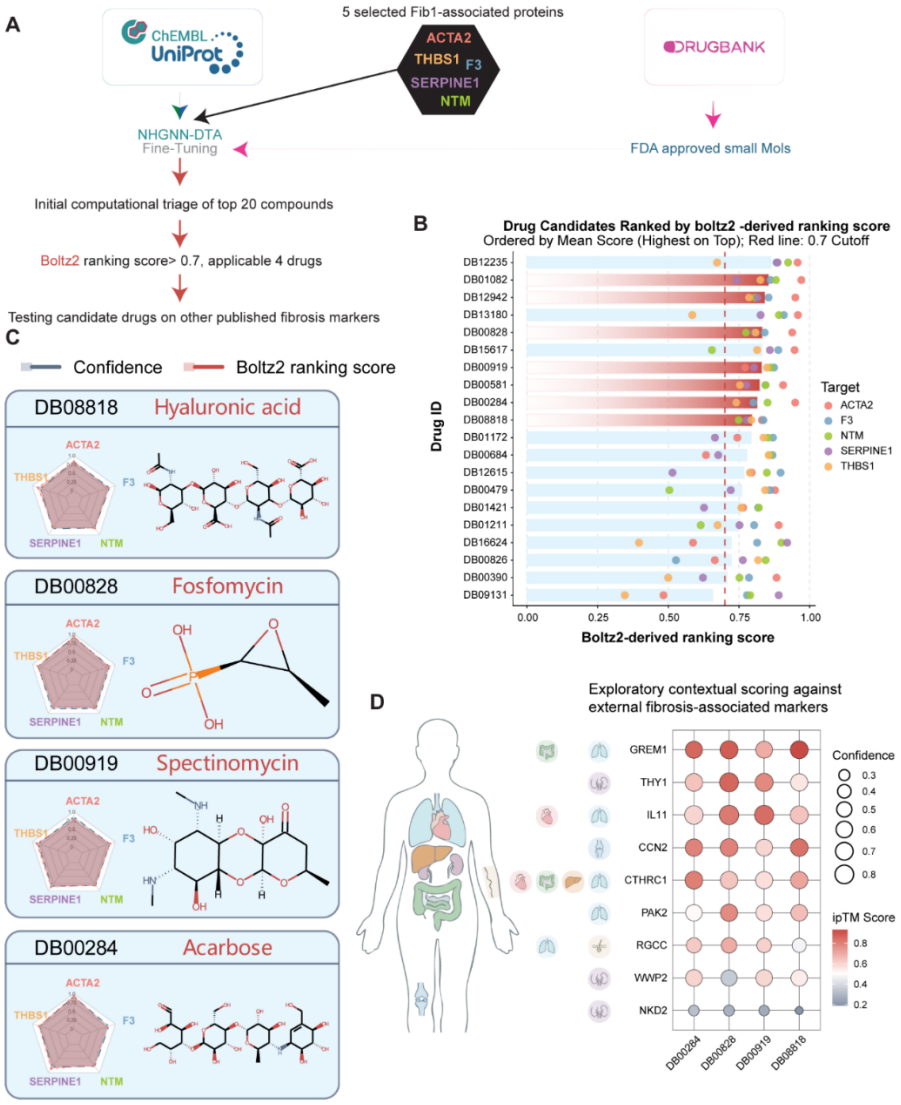

Figure 7. Exploratory computational prioritization and cross-disease scoring of FDA-approved small molecules associated with the Fib1-linked fibrotic signature. (**A**) Schematic workflow of the exploration in silico prioritization process, integrating data from ChEMBL (for drug-target affinity resources), UniProt (for protein structures), and DrugBank (for FDA-approved small-molecule metadata). The pipeline uses NHGNN-DTA for initial screening of the top 20 candidates, followed by further evaluation using Boltz2-derived structural/model outputs. (**B**) Ranking of the top 20 drug candidates based on Boltz2-derived model scores across five selected Fib1-associated proteins (ACTA2, F3, NTM, SERPINE1, and THBS1). The dashed red line indicates the prespecified model cutoff of 0.7 used as an internal exploratory retention criterion; seven compounds exceeded this threshold across all five targets, of which four (DB00284, DB00828, DB00919, and DB08818) were retained after feasibility-based filtering. (**C**) Radar plots and chemical structures of the four retained compounds (Acarbose, Fosfomycin, Spectinomycin, and Hyaluronic acid), illustrating their relative model-derived scores across the five selected proteins. The colored layers represent Boltz2 confidence scores and model scores. (**D**) Cross-disease exploratory scoring of the retained compounds. The human schematic (left) highlights organs with documented fibrotic pathologies; the corresponding dot plot (right) displays the relative Boltz2-derived model scores of the four selected compounds against established fibrosis-related markers (e.g., GREM1, IL11, CTHRC1) derived from external single-cell datasets.

Based on clinical feasibility considerations, we retained four compounds for further exploratory evaluation: Acarbose (DB00284), Fosfomycin (DB00828), Spectinomycin (DB00919), and Hyaluronic acid (DB08818) (Figure 7B). Radar plots and structural analyses showed that these four molecules had comparatively strong model-derived scores and high confidence scores across the entire Fib1-specific protein set (Figure 7C). The predicted complexes and interface visualizations are visualized in Figure S5. Finally, we evaluated the broader relevance of the prioritized compounds against established fibrotic markers derived from external single-cell studies covering diverse organ systems (Figure 7D). All four compounds showed comparatively high model-derived scores across a broad panel of fibrosis-related markers, including GREM1, IL11, CTHRC1, CCN2, and THY1 (Figure 7D). Collectively, these results yielded a prioritized set of exploratory compounds associated with the Fib1-linked fibrotic signature, providing a preliminary basis for future validation in bone nonunion and other fibroproliferative conditions.

4. Discussion

Our single-cell re-analysis suggests that the intramedullary microenvironment of bone nonunion is not merely characterized by failed regeneration, but also by an expanded fibroinflammatory program involving macrophages and fibroblasts. We identify expanded macrophage and fibroblast compartments that are skewed toward a pathological executor state. In this framework, macrophages provide the dominant profibrotic input, while a discrete fibroblast subpopulation (Fib1) concentrates the downstream response and shapes the nonunion tissue outcome. This conceptual shift maps a potential cellular trajectory of repair derailment and highlights an "immune-fibrotic lock" as a tractable hypothesis for future validation. This framework complements rather than replaces previous human transcriptomic studies of nonunion, with La Manna et al. emphasizing osteoprogenitor-associated dysregulation and Salichos et al. describing bulk tissue-level remodeling, whereas our analysis resolves intramedullary cellular heterogeneity and predicted macrophage-to-fibroblast communication. In an external reference-guided deconvolution of the published bulk cohort, we observed a numerically higher inferred fibroblast fraction in nonunion, although this trend did not reach statistical significance.

Building on this model, our results indicate that the nonunion niche reflects a failure to terminate and contextually resolve TGF-β signaling [43]. In physiological fracture repair, TGF-β activity is tightly time- and context-dependent, coordinating early mesenchymal responses and callus formation [44]. In contrast, our communication analysis points to an asymmetric signaling configuration in nonunion. Macrophages contribute enriched TGFB1 signaling, while fibroblasts display elevated expression of TGFBR1 and TGFBR2, consistent with heightened receptor sensitivity. Within the fibroblast pool, Fib1 most clearly aligns with a receiver–executor state, linking the upstream axis to downstream pathology. This receptor-level bias parallels chronic fibrotic conditions in other tissues, where differential receptor expression can amplify TGF-β signaling and favor maladaptive remodeling [45]. Importantly, unfavorable biological characteristics such as a senescent callus niche can convert increased TGF-β1 activity from supportive to inhibitory for healing [46]. Consistent with this paradigm, the TGF-β axis in our dataset is accompanied by a Fib1-centered myofibroblast-like program marked by prominent markers, such as ACTA2, SERPINE1, and THBS1 expression. Together with the subtype-resolved supplementary communication analysis, these features are consistent with a model in which macrophage-associated TGF-β signaling preferentially converges on Fib1 in nonunion and may contribute to excessive matrix deposition and impaired bridging, rather than providing direct causal proof that macrophage inputs induce Fib1 state emergence. This interpretation is also compatible with independent single-cell evidence describing fibroblast populations with high fibrogenic potential that impede callus union [47]. These observations prompted us to examine how Fib1 may sustain a high output profibrotic state once established in the nonunion microenvironment. To improve the biological interpretability of fibroblast phenotyping, we selected these phenotype axes to capture complementary dimensions of failed repair rather than to provide a generic module-scoring description. Migration- and myogenesis-related signatures were included to reflect mesenchymal recruitment/plasticity relevant to fracture repair [48,49], whereas mechanical signaling, fibrosis, and myofibroblast differentiation were prioritized because persistent matrix sensing, contractile activation, and fibrotic tissue deposition are central features of maladaptive healing and non-mineralizing scar formation [50–53]. Senescence and cell-cycle state were evaluated together because impaired fracture healing has been linked to senescent stromal/callus cells and to dysregulated cell-state transitions rather than simply productive proliferation [43,54]. In this context, the stronger disease separation observed for fibrosis-, mechanotransduction-, myofibroblast-, and senescence-related programs suggest that nonunion fibroblasts are defined primarily by pathological matrix execution and stress-associated remodeling, whereas migration-related differences appear more modest.

Rather than hinging on a single upstream regulator, our regulon-level analysis supports a convergent architecture in which multiple transcriptional programs funnel into a compact, actionable effector module.

Notably, developmental regulators that classically govern skeletal lineages can be repurposed in chronic disease to drive fibrosis across various organs, such as the SOX9- and PRRX-family programs [55,56]. While these TFs represent the "master switches" of the fibrotic identity, they are often considered high-risk therapeutic targets due to their systemic pleiotropy and the lack of traditional small-molecule binding pockets [57]. Directly perturbing such TFs poses a significant risk of off-target toxicity, as they fulfill critical homeostatic roles in non-target tissues [58]. Consequently, our strategy prioritizes the shared downstream executors (F3, THBS1, SERPINE1, ACTA2, and NTM) which operationalize the pathological phenotype and offer a more specific, druggable therapeutic window. In silico perturbation confirms that silencing this module broadly suppresses "collagen trimer" outputs without the systemic risks associated with upstream control nodes. Mechanistically, several members of this module act as profibrotic amplifiers: THBS1 reinforces TGF-β signaling by activating its latent forms, while ACTA2 enables the mechanical execution of matrix contraction [59,60]. Furthermore, SERPINE1 (PAI-1) likely acts as a master suppressor of matrix turnover, contributing to "failed regeneration" rather than transient repair [61]. This effector state is further stabilized by the extracellular context; for instance, hyaluronan-rich matrices—a feature targeted by our subsequent drug screening—are known to orchestrate the maintenance of the myofibroblast phenotype by modulating receptor organization [62]. Importantly, this effector machinery is embedded within a permissive metabolic and stress-adapted "soil". In our dataset, nonunion fibroblasts display distinct metabolic remodeling, characterized by intensified macrophage-to-fibroblast glutamine signaling via the SLC38A2 axis and an expanded senescent fraction. Such features align with broader paradigms where senescent stromal cells adopt a secretory phenotype that fuels chronic inflammation, while metabolic rewiring provides the biosynthetic capacity and redox buffering required for persistent ECM synthesis [63,64]. Direct evidence suggests that glutamine metabolism is functionally required for fibrotic execution, as its inhibition can attenuate myofibroblast differentiation [65]. Collectively, these lines of evidence support a reinforcing coupling in nonunion: a compact effector hub implements the fibrotic output, while an ECM- and metabolism-shaped microenvironment sustains the "immune-fibrotic lock". This framing defines a concrete Fib1 molecular phenotype, providing a clear rationale for the targeted translational strategy.

Guided by this framework, our exploratory therapeutic prioritization focused on Fib1 state modulation rather than broad immune manipulation. While macrophages initiate the inflammatory cue, recent bidirectional CRISPR screening supports the view that the transition to persistent fibrosis is ultimately governed by intrinsic regulatory circuits within the fibroblast itself [42]. In bone, this distinction is not merely mechanistic but a strategic necessity for therapeutic design. The initial "inflammatory burst" from macrophages is mandatory for bone repair, as these cells are essential for osteoblast recruitment and early callus mineralization; broad myeloid suppression could inadvertently derail the early regenerative window [66]. In contrast, the Fib1 effector module may represent a downstream bottleneck in nonunion. Modulating this fibroblast-intrinsic program may help alleviate the established collagenous barrier while preserving macrophage functions required for physiological repair. Accordingly, we explored a small-molecule repurposing framework with an emphasis on locally deliverable compounds, given their favorable stability, low immunogenicity, scalable manufacturing, and compatibility with depot-based delivery concepts [67,68]. Within this constrained and practically relevant space, we retained four compounds (Acarbose, Fosfomycin, Spectinomycin, and Hyaluronic acid) as exploratory priorities based on their computational ranking and feasibility for future repurposing-oriented evaluation. Acarbose has documented anti-inflammatory activity in human monocyte/macrophage systems and has also been reported to attenuate fibrosis-associated readouts in vivo, providing a plausible context for future evaluation in fibroinflammatory settings [69,70]. Fosfomycin was retained not only because of its antimicrobial relevance to complex orthopaedic settings, but also because it has reported immunomodulatory effects and achieves measurable concentrations in bone and infected soft tissues [71,72]. Spectinomycin was retained as a repurposing-compatible aminocyclitol antibiotic with a well-characterized clinical profile, although its relevance here should be regarded as exploratory and will require dedicated biological validation [73]. Finally, hyaluronic acid was retained as a clinically established musculoskeletal agent and ECM modulator; importantly, high–molecular weight hyaluronan has been reported to attenuate fibrotic scarring in injury settings, providing cross-context support for future matrix-normalizing evaluation [74]. Equally important, our exploratory screening logic incorporated a clinical safety exclusion filter. We explicitly deprioritized osmotic laxatives such as lactulose (and the related agent lactitol) because they are designed to increase intraluminal osmotic pressure and can create a local hypertonic milieu [75]. Hyperosmotic stress is not immunologically inert; macrophages can sense hypertonicity and activate inflammasome-linked inflammatory programs, raising a mechanistic concern that local exposure could aggravate tissue injury rather than resolve it [76]. Together, this framework provides a mechanistically grounded rationale for future fibroblast-centered repurposing studies. Importantly, this compound-prioritization component should be interpreted as hypothesis-generating only, because the selected Fib1-associated proteins are not uniformly conventional small-

molecule targets and no orthogonal biochemical, cellular target-engagement, or in vivo validation was performed in the present study.

Our study has several limitations: First, our conclusions are derived from re-mining a single published human intramedullary scRNA-seq cohort (femoral nonunion), with modest sample size and restricted anatomical scope; thus, the prevalence and portability of the Fib1 executor state across diverse long bones, fixation contexts, and infection-associated nonunions remain to be tested in larger, prospective collections. In addition, the relatively modest endothelial transcriptional changes observed here should not be interpreted as evidence against vascular involvement in nonunion. In atrophic nonunion, vascular impairment may be spatial, structural, or perfusion-related rather than necessarily reflected by large endothelial transcriptomic shifts, and these features may be incompletely captured by dissociated single-cell profiling of a small intramedullary cohort. Moreover, the apparent abundance of endothelial cells and their inferred interactions can be influenced by donor-level heterogeneity, tissue sampling, and dissociation-related compositional bias. Second, multiple key layers in this work, including ligand–receptor communication, metabolite-mediated coupling, and senescence quantification, are computational inferences from transcriptomes and should be validated with orthogonal evidence (e.g., spatially resolved mapping of Fib1 and its effector module, proteomic confirmation of pathway activation, and functional assays of matrix production). Third, our virtual perturbation and drug nomination pipeline provides a principled prioritization rather than causal proof: regulon inference and in silico knockouts approximate network controllability, and affinity predictions do not substitute for biochemical binding or efficacy in relevant bone-healing models. Moving forward, the most direct translational path is a staged validation program that (i) confirms Fib1 localization and persistence within the collagenous barrier, (ii) tests whether suppressing the five-gene effector module restores pro-regenerative signaling and matrix turnover ex vivo and in vivo, and (iii) evaluates locally deliverable candidate compounds in preclinical nonunion models with clinically realistic exposure and safety constraints. If successful, this framework would convert a historically descriptive view of nonunion into a targetable, fibroblast-centered disease state, enabling precision pharmacologic strategies designed to dismantle the established fibrotic blockade while preserving immune programs required for physiological repair.

Supplementary Materials

The additional data and information can be downloaded at: https://media.sciltp.com/articles/others/26042713 53133184/RMD-26020133-SI-FC.pdf. Figure S1: External comparison with the published GSE226568/GSE226566 bulk RNA-seq cohort using reference-guided deconvolution. Figure S2: Ridge plots comparing functional pathway scores (Migration, Mechanical, Fibrosis, Myofib, and Myogenesis) between control and Nonunion fibroblasts using "AUCell". Figure S3: Subtype-resolved macrophage-to-Fib1 communication in nonunion. Figure S4: Reproducibility and robustness of the Fib1-like fibroblast state in nonunion. Figure S5: Predicted binding mode of Fib1 target proteins with potential candidate drugs generated by Boltz2.

Author Contributions

H.C.: conceptualization, methodology, software, formal analysis, data curation, writing—original draft preparation; C.L.: investigation, validation, writing—reviewing and editing; X.L.: investigation, visualization, methodology; X.C.: validation, investigation; S.L.: data curation, resources; C.X.: conceptualization, project administration, funding acquisition, supervision, writing—reviewing and editing. All authors have read and agreed to the published version of the manuscript.

Funding

C.X. acknowledges the support of the Sydney Horizon Fellowship, The University of Sydney, and the support from the Biomanufacturing Incubator, Faculty of Medicine and Health, The University of Sydney.

Institutional Review Board Statement

Ethical review and approval were waived for this study because all data were obtained from publicly available, de-identified human transcriptomic datasets in the NCBI GEO database. No new human or animal subjects were involved in this research.

Informed Consent Statement

Not applicable. This study analyzed a publicly available, de-identified transcriptomic dataset from the NCBI GEO database; no new human participants were recruited or directly involved.

Data Availability Statement

All data analyzed in this study are publicly available from the NCBI Gene Expression Omnibus (GEO) under accession numbers GSE217792 and GSE226566. Processed data and analysis scripts are available from the corresponding authors upon reasonable request.

Conflicts of Interest

The authors declare no conflict of interest.

Use of AI and AI-Assisted Technologies

During the preparation of this work, the authors used ChatGPT (OpenAI) for English language polishing and grammar improvement. No AI tools are used to generate content. After using this tool, the authors reviewed and edited the content as needed and take full responsibility for the final version of the manuscript.

References

1. Vanderkarr, M.F.; Ruppenkamp, J.W.; Vanderkarr, M.; et al. Risk factors and healthcare costs associated with long bone fracture non-union: A retrospective US claims database analysis. *J. Orthop. Surg. Res.* **2023**, *18*, 745. https://doi.org/10.1186/s13018-023-04232-3.
2. Thomas, J.D.; Kehoe, J.L. Bone Nonunion. In *StatPearls*; StatPearls Publishing: Treasure Island, FL, USA, 2025.
3. Vincken, L.; van der Broeck, L.; Geurts, J.; et al. The effect of post-traumatic long bone non-unions on health-related quality of life. *Injury* **2023**, *54*, 110929. https://doi.org/10.1016/j.injury.2023.110929.
4. Saul, D.; Menger, M.M.; Ehnert, S.; et al. Bone Healing Gone Wrong: Pathological Fracture Healing and Non-Unions-Overview of Basic and Clinical Aspects and Systematic Review of Risk Factors. *Bioengineering* **2023**, *10*, 85. https://doi.org/10.3390/bioengineering10010085.
5. Capobianco, C.A.; Hankenson, K.D.; Knights, A.J. Temporal dynamics of immune-stromal cell interactions in fracture healing. *Front. Immunol.* **2024**, *15*, 1352819. https://doi.org/10.3389/fimmu.2024.1352819.
6. Wildemann, B.; Ignatius, A.; Leung, F.; et al. Non-union bone fractures. *Nat. Rev. Dis. Primers* **2021**, *7*, 57. https://doi.org/10.1038/s41572-021-00289-8.
7. Vukicevic, S.; Peric, M.; Bordukalo-Niksic, T.; et al. Time to consider fracture nonunion an orphan disease? An update into pathophysiology, epidemiology and therapeutic solutions. *Eur. J. Trauma Emerg. Surg.* **2025**, *51*, 255. https://doi.org/10.1007/s00068-025-02918-3.
8. Qin, Q.; Lee, S.; Patel, N.; et al. Neurovascular coupling in bone regeneration. *Exp. Mol. Med.* **2022**, *54*, 1844–1849. https://doi.org/10.1038/s12276-022-00899-6.
9. Panteli, M.; Pountos, I.; Jones, E.; et al. Biological and molecular profile of fracture non-union tissue: Current insights. *J. Cell. Mol. Med.* **2015**, *19*, 685–713. https://doi.org/10.1111/jcmm.12532.
10. Avin, K.G.; Dominguez, J.M., 2nd; Chen, N.X.; et al. Single-cell RNAseq provides insight into altered immune cell populations in human fracture nonunions. *J. Orthop. Res.* **2023**, *41*, 1060–1069. https://doi.org/10.1002/jor.25452.
11. La Manna, F.; Hanhart, D.; Kloen, P.; et al. Molecular profiling of osteoprogenitor cells reveals FOS as a master regulator of bone non-union. *Gene* **2023**, *874*, 147481. https://doi.org/10.1016/j.gene.2023.147481.
12. Salichos, L.; Thayavally, R.; Kloen, P.; et al. Human nonunion tissues display differential gene expression in comparison to physiological fracture callus. *Bone* **2024**, *183*, 117091. https://doi.org/10.1016/j.bone.2024.117091.
13. Hao, Y.; Stuart, T.; Kowalski, M.H.; et al. Dictionary learning for integrative, multimodal and scalable single-cell analysis. *Nat. Biotechnol.* **2024**, *42*, 293–304. https://doi.org/10.1038/s41587-023-01767-y.
14. Zeng, Z.; Ma, Y.; Hu, L.; et al. OmicVerse: A framework for bridging and deepening insights across bulk and single-cell sequencing. *Nat. Commun.* **2024**, *15*, 5983. https://doi.org/10.1038/s41467-024-50194-3.
15. Germain, P.L.; Lun, A.; Garcia Meixide, C.; et al. Doublet identification in single-cell sequencing data using scDblFinder. *F1000Res* **2021**, *10*, 979. https://doi.org/10.12688/f1000research.73600.2.
16. Korsunsky, I.; Millard, N.; Fan, J.; et al. Fast, sensitive and accurate integration of single-cell data with Harmony. *Nat. Methods* **2019**, *16*, 1289–1296. https://doi.org/10.1038/s41592-019-0619-0.
17. Dann, E.; Henderson, N.C.; Teichmann, S.A.; et al. Differential abundance testing on single-cell data using k-nearest neighbor graphs. *Nat. Biotechnol.* **2022**, *40*, 245–253. https://doi.org/10.1038/s41587-021-01033-z.
18. Chu, T.; Wang, Z.; Pe'er, D.; et al. Cell type and gene expression deconvolution with BayesPrism enables Bayesian integrative analysis across bulk and single-cell RNA sequencing in oncology. *Nat. Cancer* **2022**, *3*, 505–517. https://doi.org/10.1038/s43018-022-00356-3.

19. Jin, S.; Plikus, M.V.; Nie, Q. CellChat for systematic analysis of cell–cell communication from single-cell transcriptomics. *Nat. Protoc.* **2025**, *20*, 180–219. https://doi.org/10.1038/s41596-024-01045-4.
20. Browaeys, R.; Saelens, W.; Saeys, Y. NicheNet: Modeling intercellular communication by linking ligands to target genes. *Nat. Methods* **2020**, *17*, 159–162. https://doi.org/10.1038/s41592-019-0667-5.
21. Alghamdi, N.; Chang, W.; Dang, P.; et al. A graph neural network model to estimate cell-wise metabolic flux using single-cell RNA-seq data. *Genome Res.* **2021**, *31*, 1867–1884. https://doi.org/10.1101/gr.271205.120.
22. Zheng, R.; Zhang, Y.; Tsuji, T.; et al. MEBOCOST maps metabolite-mediated intercellular communications using single-cell RNA-seq. *Nucleic Acids Res.* **2025**, *53*, gkaf569. https://doi.org/10.1093/nar/gkaf569.
23. Wang, J.; Zhou, X.; Yu, P.; et al. A transcriptome-based human universal senescence index (hUSI) robustly predicts cellular senescence under various conditions. *Nat. Aging* **2025**, *5*, 1159–1175. https://doi.org/10.1038/s43587-025-00886-2.
24. Bauer-Rowe, K.E.; Pham, B.; Griffin, M.; et al. Creeping fat-derived mechanosensitive fibroblasts drive intestinal fibrosis in Crohn's disease strictures. *Cell* **2025**, *188*, 6536–6553.e26. https://doi.org/10.1016/j.cell.2025.08.029.
25. Aibar, S.; González-Blas, C.B.; Moerman, T.; et al. SCENIC: Single-cell regulatory network inference and clustering. *Nat. Methods* **2017**, *14*, 1083–1086. https://doi.org/10.1038/nmeth.4463.
26. Zhou, Y.; Zhou, B.; Pache, L.; et al. Metascape provides a biologist-oriented resource for the analysis of systems-level datasets. *Nat. Commun.* **2019**, *10*, 1523. https://doi.org/10.1038/s41467-019-09234-6.
27. Osorio, D.; Zhong, Y.; Li, G.; et al. scTenifoldKnk: An efficient virtual knockout tool for gene function predictions via single-cell gene regulatory network perturbation. *Patterns* **2022**, *3*, 100434. https://doi.org/10.1016/j.patter.2022.100434.
28. Liu, L.; Li, W.; Wang, F.; et al. A pre-trained large generative model for translating single-cell transcriptomes to proteomes. *Nat. Biomed. Eng.* **2025**. https://doi.org/10.1038/s41551-025-01528-z.
29. Knox, C.; Wilson, M.; Klinger, C.M.; et al. DrugBank 6.0: The DrugBank Knowledgebase for 2024. *Nucleic Acids Res.* **2024**, *52*, D1265–D1275. https://doi.org/10.1093/nar/gkad976.
30. UniProt Consortium. UniProt: The Universal Protein Knowledgebase in 2025. *Nucleic Acids Res.* **2025**, *53*, D609–D617. https://doi.org/10.1093/nar/gkae1010.
31. Zdrazil, B.; Felix, E.; Hunter, F.; et al. The ChEMBL Database in 2023: A drug discovery platform spanning multiple bioactivity data types and time periods. *Nucleic Acids Res.* **2024**, *52*, D1180–D1192. https://doi.org/10.1093/nar/gkad1004.
32. He, H.; Chen, G.; Chen, C.Y. NHGNN-DTA: A node-adaptive hybrid graph neural network for interpretable drug-target binding affinity prediction. *Bioinformatics* **2023**, *39*, btad355. https://doi.org/10.1093/bioinformatics/btad355.
33. Passaro, S.; Corso, G.; Wohlwend, J.; et al. Boltz-2: Towards Accurate and Efficient Binding Affinity Prediction. *bioRxiv* **2025**. https://doi.org/10.1101/2025.06.14.659707.
34. Li, Z.; Jiang, J.; Cai, K.; et al. CCN2 mediates fibroblast-macrophage interaction in knee arthrofibrosis based on single-cell RNA-seq analysis. *Bone Res.* **2025**, *13*, 26. https://doi.org/10.1038/s41413-025-00400-9.
35. Watanabe, N.; Yoshida, M.; Hirano, Y.; et al. Integrated spatial and single-cell transcriptomics reveal PAK kinase as a therapeutic target in fibroblastic foci and dense fibrosis of idiopathic pulmonary fibrosis. *Eur. Respir. J.* **2025**, *66*, 2400022. https://doi.org/10.1183/13993003.00022-2025.
36. Chen, H.; You, R.; Guo, J.; et al. WWP2 Regulates Renal Fibrosis and the Metabolic Reprogramming of Profibrotic Myofibroblasts. *J. Am. Soc. Nephrol.* **2024**, *35*, 696–718. https://doi.org/10.1681/asn.0000000000000328.
37. Ge, C.; Huang, M.; Han, Y.; et al. Demethyleneberberine Alleviates Pulmonary Fibrosis through Disruption of USP11 Deubiquitinating GREM1. *Pharmaceuticals* **2024**, *17*, 279. https://doi.org/10.3390/ph17030279.
38. Luzina, I.G.; Rus, V.; Lockatell, V.; et al. Regulator of Cell Cycle Protein (RGCC/RGC-32) Protects against Pulmonary Fibrosis. *Am. J. Respir. Cell Mol. Biol.* **2022**, *66*, 146–157. https://doi.org/10.1165/rcmb.2021-0022OC.
39. Zhou, J.; An, X.; Xia, X.; et al. Aging-associated interleukin-11 drives the molecular mechanism and targeted therapy of idiopathic pulmonary fibrosis. *Eur. J. Med. Res.* **2025**, *30*, 542. https://doi.org/10.1186/s40001-025-02755-5.
40. Kuppe, C.; Ibrahim, M.M.; Kranz, J.; et al. Decoding myofibroblast origins in human kidney fibrosis. *Nature* **2021**, *589*, 281–286. https://doi.org/10.1038/s41586-020-2941-1.
41. Li, L.; Tao, M.; Gao, X.; et al. Uncovering key markers and therapeutic targets for renal fibrosis in diabetic kidney disease through bulk and single-cell RNA sequencing. *J. Transl. Med.* **2025**, *23*, 742. https://doi.org/10.1186/s12967-025-06554-8.
42. Pokatayev, V.; Jaiswal, A.; Shih, A.R.; et al. Bidirectional CRISPR screens decode a GLIS3-dependent fibrotic cell circuit. *Nature* **2026**, *650*, 997–1006. https://doi.org/10.1038/s41586-025-09907-x.
43. Liu, J.; Zhang, J.; Lin, X.; et al. Age-associated callus senescent cells produce TGF-β1 that inhibits fracture healing in aged mice. *J. Clin. Investig.* **2022**, *132*, e148073. https://doi.org/10.1172/jci148073.
44. Wu, M.; Wu, S.; Chen, W.; et al. The roles and regulatory mechanisms of TGF-β and BMP signaling in bone and cartilage development, homeostasis and disease. *Cell Res.* **2024**, *34*, 101–123. https://doi.org/10.1038/s41422-023-00918-9.
45. Khalil, N.; Parekh, T.V.; O'Connor, R.; et al. Regulation of the effects of TGF-β1 by activation of latent TGF-β1 and differential expression of TGF-β receptors (TβR-I and TβR-II) in idiopathic pulmonary fibrosis. *Thorax* **2001**, *56*, 907–915. https://doi.org/10.1136/thorax.56.12.907.

46. Zheng, N.; Xu, J.; Ruan, Y.C.; et al. Magnesium facilitates the healing of atypical femoral fractures: A single-cell transcriptomic study. *Mater. Today* **2022**, *52*, 43–62. https://doi.org/10.1016/j.mattod.2021.11.028.
47. Bowers, K.M.; Anderson, D.E. Delayed Union and Nonunion: Current Concepts, Prevention, and Correction: A Review. *Bioengineering* **2024**, *11*, 525. https://doi.org/10.3390/bioengineering11060525.
48. Julien, A.; Kanagalingam, A.; Martínez-Sarrà, E.; et al. Direct contribution of skeletal muscle mesenchymal progenitors to bone repair. *Nat. Commun.* **2021**, *12*, 2860. https://doi.org/10.1038/s41467-021-22842-5.
49. He, Q.; Lu, J.; Liang, Q.; et al. Prg4+ fibroadipogenic progenitors in muscle are crucial for bone fracture repair. *Proc. Natl. Acad. Sci. U.S.A.* **2025**, *122*, e2417806122. https://doi.org/10.1073/pnas.2417806122.
50. Dupont, S.; Morsut, L.; Aragona, M.; et al. Role of YAP/TAZ in mechanotransduction. *Nature* **2011**, *474*, 179–183. https://doi.org/10.1038/nature10137.
51. Tai, Y.; Woods, E.L.; Dally, J.; et al. Myofibroblasts: Function, Formation, and Scope of Molecular Therapies for Skin Fibrosis. *Biomolecules* **2021**, *11*, 1095. https://doi.org/10.3390/biom11081095.
52. Huang, F.; Wei, G.; Wang, H.; et al. Fibroblasts inhibit osteogenesis by regulating nuclear-cytoplasmic shuttling of YAP in mesenchymal stem cells and secreting DKK1. *Biol. Res.* **2024**, *57*, 4. https://doi.org/10.1186/s40659-023-00481-y.
53. Wang, L.; Tower, R.J.; Chandra, A.; et al. Periosteal Mesenchymal Progenitor Dysfunction and Extraskeletally-Derived Fibrosis Contribute to Atrophic Fracture Nonunion. *J. Bone Miner. Res.* **2019**, *34*, 520–532. https://doi.org/10.1002/jbmr.3626.
54. Saul, D.; Monroe, D.G.; Rowsey, J.L.; et al. Modulation of fracture healing by the transient accumulation of senescent cells. *eLife* **2021**, *10*, e69958. https://doi.org/10.7554/eLife.69958.
55. Trogisch, F.A.; Abouissa, A.; Keles, M.; et al. Endothelial cells drive organ fibrosis in mice by inducing expression of the transcription factor SOX9. *Sci. Transl. Med.* **2024**, *16*, eabq4581. https://doi.org/10.1126/scitranslmed.abq4581.
56. Bai, W.W.; Tang, Z.Y.; Shan, T.C.; et al. Up-regulation of paired-related homeobox 2 promotes cardiac fibrosis in mice following myocardial infarction by targeting of Wnt5a. *J. Cell. Mol. Med.* **2020**, *24*, 2319–2329. https://doi.org/10.1111/jcmm.14914.
57. Henley, M.J.; Koehler, A.N. Advances in targeting 'undruggable' transcription factors with small molecules. *Nat. Rev. Drug Discov.* **2021**, *20*, 669–688. https://doi.org/10.1038/s41573-021-00199-0.
58. Joris, V.; Schumacher, A.; Marks, M.P.; et al. FGF9 treatment reduces off-target chondrocytes from iPSC-derived kidney organoids. *npj Regen. Med.* **2025**, *10*, 41. https://doi.org/10.1038/s41536-025-00428-9.
59. Blanco-Mezquita, J.T.; Hutcheon, A.E.; Zieske, J.D. Role of thrombospondin-1 in repair of penetrating corneal wounds. *Investig. Ophthalmol. Vis. Sci.* **2013**, *54*, 6262–6268. https://doi.org/10.1167/iovs.13-11710.
60. Shinde, A.V.; Humeres, C.; Frangogiannis, N.G. The role of α-smooth muscle actin in fibroblast-mediated matrix contraction and remodeling. *Biochim. Biophys. Acta Mol. Basis Dis.* **2017**, *1863*, 298–309. https://doi.org/10.1016/j.bbadis.2016.11.006.
61. Simone, T.M.; Higgins, C.E.; Czekay, R.P.; et al. SERPINE1: A Molecular Switch in the Proliferation-Migration Dichotomy in Wound-"Activated" Keratinocytes. *Adv. Wound Care* **2014**, *3*, 281–290. https://doi.org/10.1089/wound.2013.0512.
62. Webber, J.; Meran, S.; Steadman, R.; et al. Hyaluronan orchestrates transforming growth factor-β1-dependent maintenance of myofibroblast phenotype. *J. Biol. Chem.* **2009**, *284*, 9083–9092. https://doi.org/10.1074/jbc.M806989200.
63. Wang, B.; Han, J.; Elisseeff, J.H.; et al. The senescence-associated secretory phenotype and its physiological and pathological implications. *Nat. Rev. Mol. Cell Biol.* **2024**, *25*, 958–978. https://doi.org/10.1038/s41580-024-00727-x.
64. Feng, L.; Chen, X.; Huang, Y.; et al. Immunometabolism changes in fibrosis: From mechanisms to therapeutic strategies. *Front. Pharmacol.* **2023**, *14*, 1243675. https://doi.org/10.3389/fphar.2023.1243675.
65. Farah, H.; Young, S.P.; Mauro, C.; et al. Metabolic dysfunction and inflammatory disease: The role of stromal fibroblasts. *FEBS J.* **2021**, *288*, 5555–5568. https://doi.org/10.1111/febs.15644.
66. Schlundt, C.; El Khassawna, T.; Serra, A.; et al. Macrophages in bone fracture healing: Their essential role in endochondral ossification. *Bone* **2018**, *106*, 78–89. https://doi.org/10.1016/j.bone.2015.10.019.
67. Cherief, M.; Xu, J.; Li, Z.; et al. TrkA-mediated sensory innervation of injured mouse tendon supports tendon sheath progenitor cell expansion and tendon repair. *Sci. Transl. Med.* **2023**, *15*, eade4619. https://doi.org/10.1126/scitranslmed.ade4619.
68. Laurencin, C.T.; Ashe, K.M.; Henry, N.; et al. Delivery of small molecules for bone regenerative engineering: Preclinical studies and potential clinical applications. *Drug Discov. Today* **2014**, *19*, 794–800. https://doi.org/10.1016/j.drudis.2014.01.012.
69. Li, X.; Zheng, S.; Xu, H.; et al. The direct and indirect inhibition of proinflammatory adipose tissue macrophages by acarbose in diet-induced obesity. *Cell Rep. Med.* **2025**, *6*, 101883. https://doi.org/10.1016/j.xcrm.2024.101883.
70. Hung, T.W.; Yu, M.H.; Yang, T.Y.; et al. Acarbose Protects Glucolipotoxicity-Induced Diabetic Nephropathy by Inhibiting Ras Expression in High-Fat Diet-Fed *db/db* Mice. *Int. J. Mol. Sci.* **2022**, *23*, 15312. https://doi.org/10.3390/ijms232315312.
71. Zeitlinger, M.; Marsik, C.; Steiner, I.; et al. Immunomodulatory effects of fosfomycin in an endotoxin model in human blood. *J. Antimicrob. Chemother.* **2007**, *59*, 219–223. https://doi.org/10.1093/jac/dkl464.

72. Schintler, M.V.; Traunmüller, F.; Metzler, J.; et al. High fosfomycin concentrations in bone and peripheral soft tissue in diabetic patients presenting with bacterial foot infection. *J. Antimicrob. Chemother.* **2009**, *64*, 574–578. https://doi.org/10.1093/jac/dkp230.
73. Lam, T.; Brennan, M.D.; Morrison, D.A.; et al. Femtoliter droplet confinement of *Streptococcus pneumoniae*: Bacterial genetic transformation by cell-cell interaction in droplets. *Lab Chip* **2019**, *19*, 682–692. https://doi.org/10.1039/c8lc01367e.
74. Wang, X.; Balaji, S.; Steen, E.H.; et al. High-molecular weight hyaluronan attenuates tubulointerstitial scarring in kidney injury. *JCI Insight* **2020**, *5*, e136345. https://doi.org/10.1172/jci.insight.136345.
75. Schumann, C. Medical, nutritional and technological properties of lactulose. An update. *Eur. J. Nutr.* **2002**, *41*, I17–I25. https://doi.org/10.1007/s00394-002-1103-6.
76. Ip, W.K.; Medzhitov, R. Macrophages monitor tissue osmolarity and induce inflammatory response through NLRP3 and NLRC4 inflammasome activation. *Nat. Commun.* **2015**, *6*, 6931. https://doi.org/10.1038/ncomms7931.